Article

Biocorona Formation and Hemolytic Effects of Graphene Oxide-Silver Nanoparticles

Nathalia C. L. Azevedo, [a] Aline M. Z. de Medeiros, [a,b] Gabriela H. da Silva, [a]
Milena L. Brito, [a,b] João M. L. Faria, [a] Fabrício S. Delite, [a]
Amauri J. Paula [c,d] and Diego S. T. Martinez *,[a,b]

[a]*Laboratório Nacional de Nanotecnologia (LNNano),
Centro Nacional de Pesquisa em Energia e Materiais (CNPEM), 13083-100 Campinas-SP, Brazil*

[b]*Centro de Energia Nuclear na Agricultura (CENA), Universidade de São Paulo (USP),
13400-970 Piracicaba-SP, Brazil*

[c]*Ilum Escola de Ciência, Centro Nacional de Pesquisa em Energia e Materiais (CNPEM),
13083-100 Campinas-SP, Brazil*

[d]*Departamento de Física, Universidade Federal do Ceará (UFC), 60440-900 Fortaleza-CE, Brazil*

The graphene oxide (GO)-silver nanoparticles (AgNPs) hybrid material (GO-AgNPs) has garnered significant interest due to its ability to combine the unique properties of GO and AgNPs, showing promise applications in biomedicine, nanocomposites, biosensors, and antimicrobial materials. However, further investigation is needed to understand the nanobio-interactions and toxicity of GO-AgNPs nanohybrid. Assessing the toxicity of GO-AgNPs on red blood cells (hemolysis) and its interactions with blood biomolecules (biocorona formation) is mandatory for biomedical applications and safety evaluation of this material. In this work, we investigate the biocorona formation associated with GO-AgNPs after interaction with human plasma and hemolysate biomolecules linked to its hemolytic effects. Both GO and GO-AgNPs exhibited a dose-dependent hemolytic effect, with GO-AgNPs showing three times greater hemolysis than GO. Nonetheless, biocorona formation fully mitigated the hemolytic effect of both materials, however, morphological damages in red blood cells may occur yet. Our findings show that biocorona formation dramatically changes the surface chemistry, colloidal behavior and toxicity of this hybrid material. Finally, this work contributes to understanding how graphene-silver nanoparticles interact with blood components to design strategies to minimize toxicity risks and enhance their applications in biomedicine and nanobiotechnology.

Keywords: nanomaterials, nanotoxicology, hemolysis, erythrocyte membrane

Introduction

Graphene oxide (GO) has attracted interest in many biomedical applications such as antimicrobial materials, biosensors, composites, drug delivery systems, and others.[1-3] GO is a two-dimensional carbon material with hexagonally arranged atoms, forming a graphene monolayer characterized by hydrophilic oxygenated functional groups.[4,5] GO is a platform to functionalize or decorate with other nanoparticles (NPs) and/or organic coatings, improving or giving new functionalities to the nanohybrid.[6-9] GO-silver NPs hybrid material (GO-AgNPs) has garnered significant interest as it combines the unique properties of both GO and AgNPs, resulting in a nanohybrid with enhanced and/or new functionalities compared to its pristine precursors.[10-19]

The combination of GO and AgNPs has shown promising applications across various fields.[20] Therefore, the production of this hybrid material has been increasingly encouraged. Consequently, the concerns about their toxicity have grown. It is known that the toxic profile of nanohybrids could differ from their counterparts. For instance, Zhou *et al.*[21] reported that GO-AuNPs (GO-gold NPs hybrid material) and GO-AgNPs exhibited higher cytotoxicity to A549 and

HepG2 cancer cells than AuNPs and AgNPs. Additionally, Tang *et al.*[22] demonstrated a greater antimicrobial activity of GO-AgNPs than AgNPs. This increased effectiveness was attributed to the disruption of the *Escherichia coli* cell wall and the inhibition of cell division in *Staphylococcus aureus*. Therefore, even though the toxic profile of GO and AgNPs have been reported, the risks associated with GO-AgNPs still need further investigation.

The use of GO-AgNPs for biomedical applications has been standing out.[8,12,18] For example, Zhou *et al.*[12] showed the potential of this material as a wound healing material with antimicrobial properties. As the circulatory system is the gateway to the human body, it is necessary to understand the interactions that nanomaterials (NMs) will have with blood components, their biocompatibility and safety aspects, especially when considering biomedical applications.[23-25]

The human blood is a complex physiological environment, comprising approximately 55% plasma, 45% red blood cells (RBCs) and less than 1% buffy coat (platelets and leukocytes). The plasma, the most abundant component in blood, is comprised of 91% water, 7% proteins and > 2% electrolytes, vitamins, metabolites, and others. More than 200 proteins are identified in human plasma, with albumin (molecular weight of approximately 66.5 kDa) being the most abundant protein.[26,27] Besides, the RBCs durability in the bloodstream is approximately 120 days, after this time, cell lysis occurs (process denominated hemolysis) and releases the hemoglobin (Hb), lipoproteins and membrane lipids, among others, from the intracellular environment.[28,29] Thus, when NMs enter the circulatory system, they can interact with biomolecules in the blood, spontaneously, forming a coating on their surface, called biocorona (composed of soft and hard corona).[30-32] The biocorona provides a biological identity to the NMs and the composition of this coating can influence their physicochemical properties.[33-35] Furthermore, the coating of biomolecules formed on the NMs surface will become the first surface of contact with cells, modulating their biological response.[36]

An important tool for evaluating nanotoxicity is the hemolysis assay, an easy and low-cost assay that provides relevant information about the toxicity of NMs. This assay quantified the release of Hb after RBCs interaction with NMs.[37-39] The effect that NM can cause on cells can be strongly related to its physical-chemical properties. Therefore, an integrated material characterization is essential to understand the toxicological impact of NMs; including information about particle composition, size distribution, shape, surface charge, surface area, surface chemistry, and aggregation, among others.[40]

In this work, we investigate the biocorona formation on GO-AgNPs nanohybrid linked to its hemolytic effect for the first time. To date, studies on the interaction of NMs with the hemolysate biomolecules (i.e., a pool of biomolecules released by RBCs during hemolysis) have been neglected. Consequently, two types of biocorona were examined: plasma biocorona, as it represents the predominant component in blood, and hemolysate biocorona. The interaction among materials, biomolecules and cells was characterized by biochemical, spectroscopical and microscopical techniques.

Experimental

Nanomaterials synthesis

The GO and GO-AgNPs were synthesized and characterized in detail in previous work by de Medeiros *et al.*[11] Briefly, the GO was synthesized by the modified Hummers method, which involves the oxidation and exfoliation of graphite using H_2SO_4 and $KMnO_4$. For the GO-AgNPs, the silver ions (Ag^+) were reduced using $NaBH_4$ in the presence of GO.

Biomolecules stocks preparation

Human plasma and RBCs concentrated (type AB^+) were provided by the Hemocenter (research project No. 40230002) from the Universidade Estadual de Campinas (UNICAMP, Brazil). The research project was previously submitted to Plataforma Brasil to obtain these biological fluids and evaluated by the UNICAMP Research Ethics Committee (Ethical assessment of research project No. 62880022.0.0000.5404). To separate the plasma lipid fraction and prepare plasma protein stocks, an aliquot was centrifuged (ROTINA 380 R centrifuge, Hettich, Tuttlingen, Germany) at 14,000 rpm for 30 min at 4 °C. For the hemolysate preparation, RBCs were centrifuged at 10,000 rpm for 10 min at 4 °C twice to remove the Hb released naturally in the RBC due to storage time. Then, the pellet was diluted with ultrapure water (UPW) and left under magnetic stirring for 1 h. The sample was centrifuged at 14,000 rpm for 30 min at 4 °C to separate the lipid membrane debris from the hemolysate. The concentration of proteins in the plasma and hemolysate was measured by Bradford (Sigma-Aldrich, Saint Louis, USA), and a stock with the concentration of 10 and 5 mg mL^{-1} of plasma and hemolysate were prepared. Both plasma and hemolysate supernatant were collected and the stock of proteins was stored at –20 °C.

Biomolecules adsorption assay

For the adsorption assay, NMs were incubated with either plasma or hemolysate for 1 h at 37 °C, followed by centrifugation at 10,000 rpm for 10 min at 4 °C. After centrifugation, for plasma adsorption assay, 5 μL of supernatant was transferred to a 96-well plate and 250 μL of Bradford was added, and after 20 min of incubation, absorption at 595 nm was obtained by reading the ultraviolet-visible (UV-Vis) spectrum on a Multiskan GO™ microplate spectrophotometer (Thermo Fisher Scientific, Vantaa, Finland). For the hemolysate adsorption assay, as the biofluid was bright red, the adsorption was obtained by reading the supernatant at 540 nm in UV-Vis. Phosphate-buffered saline (10 mmol L^{-1}) (PBS; Invitrogen, Frederick, USA) and a biomolecules dispersion at 1.0 mg mL^{-1} (plasma or hemolysate) were used as positive control (PC) and negative control (NC), respectively.

Biocorona formation and characterization

The methodology used for the biocorona formation on the GO and GO-AgNPs surface was based on Rahman *et al.*[41] GO and GO-AgNPs dispersions (0.1 mg mL^{-1}) were incubated with either 1.0 mg mL^{-1} of plasma proteins or hemolysate in a thermoblock system (Thermomixer C, Eppendorf, Hamburg, Germany) for 1 h at 4 °C. After incubation, the NM were centrifuged at 14,000 rpm for 1 h at 4 °C, followed by three washing steps (14,000 rpm for 30 min at 4 °C) with 1 mmol L^{-1} of PBS. The NM@biocorona complexes formed were stored at 4 °C and used within three days for further characterization and hemolysis assay. GO and GO-AgNPs coated by plasma proteins were designated GO@P and GO-AgNPs@P, respectively, whereas the coated NMs with hemolysate were named GO@H and GO-AgNPs@H, respectively. Furthermore, the biocorona formation was confirmed by sodium dodecyl-sulfate polyacrylamide gel electrophoresis (SDS-PAGE) and the protein profile of the hard corona was evaluated. Briefly, 40 μL of 2× Laemmli sample buffer (Bio-Rad, Hercules, USA) and 10 μL of dithiothreitol (DTT; Sigma-Aldrich, Saint Louis, USA) were applied to break the proteins bands and the samples were sonicated for 2 min and incubated at 99 °C for 3 min. Then, 10 μL of the samples were loaded on SDS-PAGE polyacrylamide gel (4% stacking gel and 15% loading gel) and 5 μL of molecular weight standard (Precision Plus Protein™ Kaleidoscope™ standards, Bio-Rad, Hercules, USA). Proteins extracted from plasma and hemolysate were added to the gel as a control. The gels were stained with Coomassie blue and scanned for biocorona profile analysis (Epson ImageScanner III, GE Healthcare, Tokyo, Japan).

Herein, the GO and GO-AgNPs coated with plasma proteins and hemolysate were evaluated using different characterization techniques. To evaluate the shape, thickness, and roughness of NMs, surface topography images were performed by atomic force microscopy (AFM; MultiMode 8-HR, Bruker, Santa Barbara, USA) in ambient conditions with a Nano Scope 5 controller and using PeakForce Tapping technology. The images obtained were processed in Gwyddion software (version 2.61)[42] and analyzed by ImageJ software.[43] Surface chemistries were analyzed by X-ray photoelectron spectroscopic (XPS; Thermo Fisher Scientific, Waltham, USA) using a monochromated, micro-focused, low-power Al K-Alpha X-ray source. The XPS data was processed in Thermo Avantage Data System (version 5.957). Fourier-transform infrared spectroscopy (FTIR) model IRSpirit (Shimadzu, Kyoto, Japan) with attenuated total reflectance (ATR) was used to obtain semi-quantitative information on the chemical groups present on the surface of the NMs.

For the colloidal stability of GO and GO-AgNPs (with and without biocorona), the absorbance was monitored from 0 to 60 min. Dispersions (1 mL) of GO and GO-AgNPs at 150 μg mL^{-1} were prepared in triplicate in UPW or 10 mmol L^{-1} of PBS. Then, the supernatant (100 μL) was collected following settling at each time interval (15 min) and the absorbance was measured by UV-Vis microplate reader at 400 nm. The assays were carried out in independent triplicates.

Hemolytic assays

Briefly, the RBCs were centrifuged at 10,000 rpm for 10 min at 4 °C, the supernatant was discarded, and the pellet was washed three times by resuspending it in 10 mmol L^{-1} of PBS. Then, an RBCs suspension (V_{final} = 1 mL), consisting of 1% (v/v) RBCs in PBS, was prepared and incubated for 1 h at 37 °C with GO or GO-AgNPs (with and without biocorona), with a concentration range from 25 to 150 μg mL^{-1}. A PC (100% hemolysis) was prepared to break the erythrocyte membrane using a hypotonic medium (UPW) and an NC (without hemolysis) with RBCs was kept in PBS. After incubation, the microtubes were centrifuged at 10,000 rpm for 10 min at 4 °C and 100 μL of supernatant of each sample was transferred to a 96-well plate. This assay was carried out in triplicates. The Hb release was read at 540 nm in UV-Vis and the hemolysis percent was calculated following the equation 1:

$$\text{Hemolysis}\,(\%) = \frac{\left(\begin{array}{c}\text{sample}\\\text{absorbance}\end{array}\right) - \left(\begin{array}{c}\text{negative control}\\\text{absorbance}\end{array}\right)}{\left(\begin{array}{c}\text{positive control}\\\text{absorbance}\end{array}\right) - \left(\begin{array}{c}\text{negative control}\\\text{absorbance}\end{array}\right)} \times 100 \quad (1)$$

J. Braz. Chem. Soc. **2024**, *35*, 12, e-20240148

3 of 14

Red blood cells morphology

The RBCs morphology after NMs interaction was evaluated by high-quality phase contrast microscopy (HQPCM; Primostar 3, ZEISS, Jena, Germany) and scanning electron microscopy (SEM; FEI Quanta 650 FEG, Thermo Fisher Scientific, Brno-Černovice, Czech Republic). For HQPCM evaluation, RBCs were incubated at 37 °C for 1 h with GO and GO-AgNPs (with and without biocorona) at 100 μg mL^{-1}. The RBCs incubation procedure was the same as that used for the hemolysis assays. After incubation, the samples were slowly homogenized, and 10 μL were collected and dripped onto a slide to perform a blood smear. The slides were evaluated by HQPCM under a 40× magnification lens and the images were captured by the ZEISS software. The RBCs diameter was measured using ImageJ software.[43] Sample preparation for SEM analysis was based on the modified protocol of Geekiyanage *et al.*[44] The RBCs were suspended in 15 mmol L^{-1} of NaCl solution and adhered on poly-D-lysine coated slides. Subsequently samples were washed twice with NaCl solution and incubated in cacodylate buffer 0.1 mol L^{-1}. Afterwards, the slides were washed once in UPW and dehydrated in 10 min steps of growing ethanol concentrations followed by 24 h incubation in hexamethyltiisilizane (HMDS) to complete dehydration. The dehydrated samples were transferred to an aluminum stub and coated with a thin carbon film (carbon evaporator, SCD 050, Bal-Tec) of approximately 10 nm. The images were acquired at different magnifications by SEM, operated with a beam acceleration voltage of 2 kV, using an Everhart-Thorley type secondary electron detector.

Data analysis

Data from hemolysis and adsorption were analyzed statistically using OriginPro 2022b software (version 9.95).[45] All data were first tested for normality using the Kolmogorov-Smirnov test and for homogeneity of variance by Brown-Forsythe test. When parameter assumptions of normal distribution were met, analysis of variance (ANOVA) was followed by Tukey's *post hoc* test to compare data. As the assumptions were unmet, data were analyzed by Kruskal-Wallis non-parametric test followed by Dunn's *post hoc* test of multiple comparisons. In the case of the hemolysis results of GO, GO-AgNPs@P and GO-AgNPs@H, the assumptions of homogeneity of variance were not met. However, ANOVA is robust to violations of the assumption of homogeneity of variance when the sample sizes are equal, thus we proceed with

the analysis.[46] The results were expressed as mean ± SD (standard deviation) and the statistical significance adopted were *p* < 0.05.

Results and Discussion

### Biomolecule adsorption and hard corona profile

Due to their large surface area NMs have a high potential to adsorb biomolecules. Our results showed that both GO and GO-AgNPs can adsorb biomolecules present in the plasma and hemolysate, being this adsorption dose-dependent (Figures 1a and 1b). Besides, statistical analysis showed that GO has a higher potential to adsorb plasma proteins than hemolysate. The same cannot be said for GO-AgNPs, for which the adsorption of plasma and hemolysate biomolecules was not statistically different. In the C 1s high-resolution XPS spectra we observed a decrease in the signals of epoxy/hydroxyl groups (C–O) and carboxyl/ester groups (C=O) when comparing GO and GO-AgNPs, indicating a reduction in the oxygenated groups of GO-AgNPs (Figure 2 and Table S1, presented in the Supplementary Information (SI) section). The oxygenated groups present on the NMs surface are used as binding sites for biomolecules, e.g., plasma proteins.[30,47] Thus, explaining the lower biomolecule adsorption observed in GO-AgNPs exposure.

We also analyzed the protein profile of the acquired hard corona coatings of the NMs by SDS-PAGE (Figures 1c and 1d). Although albumin is the most abundant protein in plasma, it is not the most intense protein band observed in the hard corona profile of GO@P and GO-AgNPs@P (Figure 1c). This occurs because the physicochemical characteristics of each NM surface influence the degree of NM-biomolecule affinity.[36] In the case of the GO@H and GO-AgNPs@H, the profile observed was similar to the profile of the hemolysate, where an intense band was observed between 15 to 10 kDa, this band can be assigned to the Hb monomer (Figure 1d).

Surface physicochemical changes after biocorona formation

Topographic analyses by AFM (Figure 3 and Figure S1, SI section) showed an increase in the thickness and roughness of the NMs@biocorona complexes in relation to bare GO and bare GO-AgNPs. An increase in GO and GO-AgNPs height of approximately 4.0 and 7.0 nm, respectively, was observed after biocorona formation. Both GO-AgNPs@P and GO-AgNPs@H showed a significant increase in thickness and roughness compared to GO@P and GO@H. However, no significant difference was
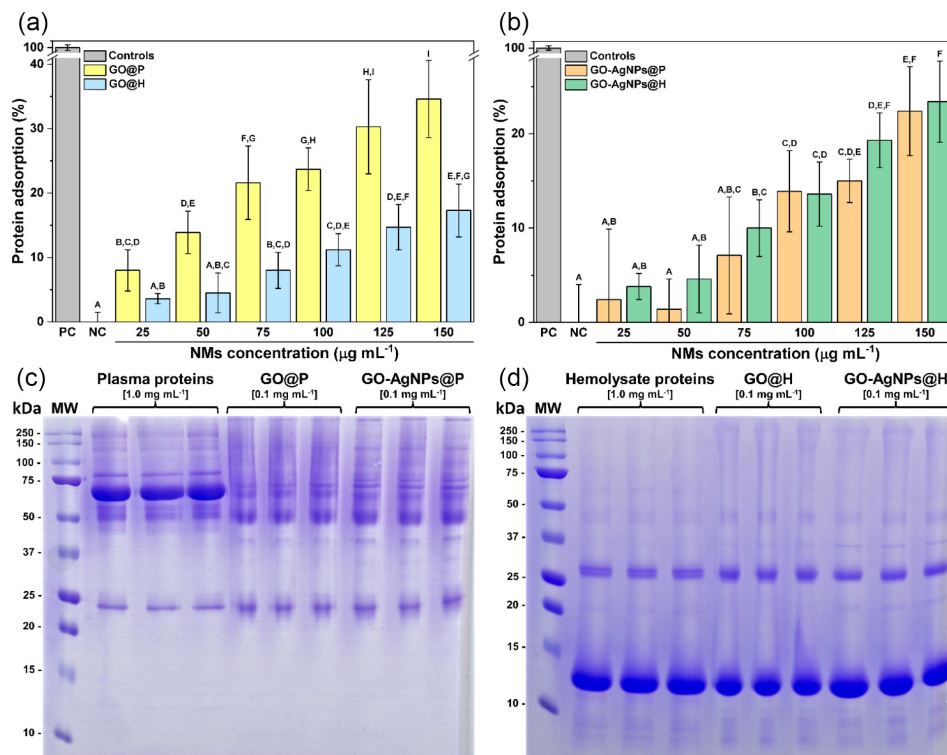
Figure 1. Protein adsorption (in %) on GO (a) and GO-AgNPs (b) after incubation with plasma and hemolysate. PC stands for only PBS and NC stands for only dispersed proteins. SDS-PAGE gels of proteins extracted from the hard corona of GO and GO-AgNPs with plasma proteins (c) and hemolysate (d). Two-way ANOVA followed by Tukey's *post hoc* test; different letters indicate significant differences ($p < 0.05$). PC: positive control, PBS: phosphate-buffered saline, NC: negative control, SDS-PAGE: sodium dodecyl-sulfate polyacrylamide gel electrophoresis.

observed between GO@P and GO@H, as well as between GO-AgNPs@P and GO-AgNPs@H.

The changes on the surface composition of the GO and GO-AgNPs after biocorona formation were analyzed by XPS (Figure 2 and Table S1, SI section). In the survey spectrum for NMs@biocorona complexes, the appearance of N 1s signals indicates the presence of biomolecules rich in nitrogenated and amino groups (Figures 2b-2c, 2e-2f). Similarly, the increase in the C 1s/O 1s intensity ratio on GO@P, GO@H, GO-AgNPs@P, and GO-AgNPs@H survey spectra indicate the increase of less oxidated organic matter adsorbed on the NMs surface, which corroborates with the biocorona formation in these surfaces (Figures 2b-2c, 2e-2f). In GO and GO-AgNPs survey spectra after biocorona formation (Figures 2a-2f), the oxygen percent on NMs surface was significantly reduced whereas nitrogen percent increased. Besides, a reduction in available silver was observed on the surface of GO-AgNPs@P and GO-AgNPs@H in relation to GO-AgNPs, due to the complete coating of their surface by biomolecules, as observed in the AFM images (Figures 3d-3f and Figures S1b, S1d, S1f, SI section). The deconvolution of GO@P, GO@H, GO-AgNPs@P, and GO-AgNPs@H C 1s high-resolution XPS spectra show signals of –C–C– (aliphatic carbon), C–O and C=O, at

284.9, 286.3 and 288.1 eV, respectively (Figures 2g-2l). The reduction of signal intensity in 286 and 288 eV indicates a reduction of the oxidized groups on the chemical surface of these NMs. That occurs due to the adsorption of the biomolecule on GO and GO-AgNPs surfaces, which are less oxidized organic matter. The Ag 3d high-resolution XPS spectrum of the GO-AgNPs, GO-AgNPs@P, and GO-AgNPs@H samples show two peaks from the 3d spin-orbital coupling on Ag electronic levels (Figures 2m-2o). The peak at 368.2 eV corresponds to the Ag $3d_{5/2}$ component, and the peak at 374.2 eV corresponds to the Ag $3d_{3/2}$ component. These results confirm a significant amount of silver deposited on the GO sheet.

The process of GO sheets functionalization with AgNPs induced a chemical reduction of the bare GO sheets, which is visualized by the reduction in intensity of the bands between 3800 and 2800 cm^{-1} and the band between 1750 and 1500 cm^{-1} in the GO-AgNPs spectrum. Also, the intensity of the peak at 1000 cm^{-1} (C–O stretching (v)) was higher for GO-AgNPs compared to the GO, suggesting a reduction due to the insertion of AgNPs (Figure 4). The analysis of attenuated total reflectance with Fourier transform infrared spectroscopy (ATR-FTIR) can detect signals from the sample surface, once the biomolecules cover the NMs
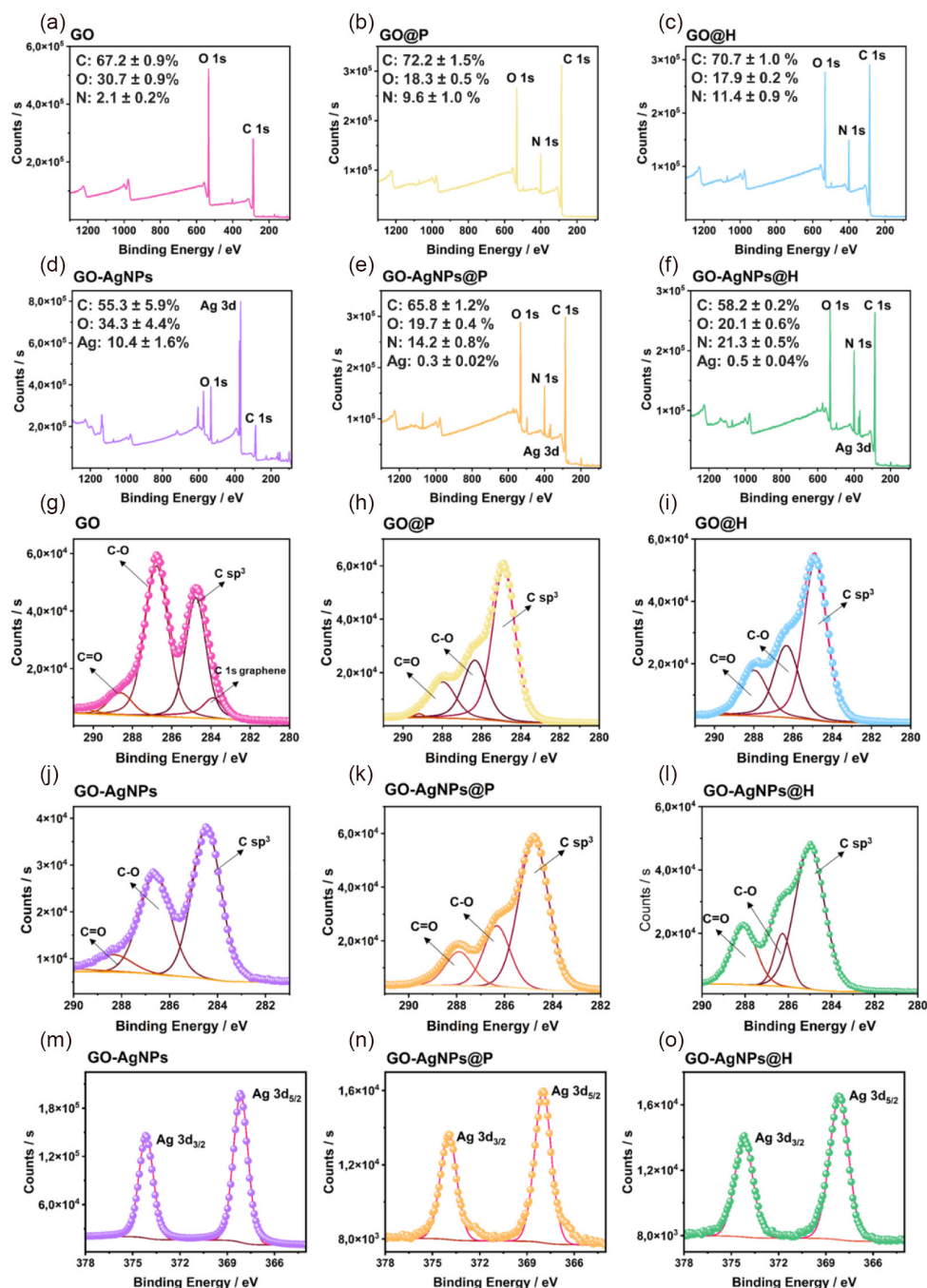
Figure 2. XPS survey spectra of GO (a), GO@P (b) and GO@H (c), GO-AgNPs (d), GO-AgNPs@P (e) and GO-AgNPs@H (f). The percentage of the elements (C, carbon; O, oxygen; N, nitrogen; Ag, silver) present on the NMs surface is represented by mean ± SD. Surface chemistry elemental analysis in high-resolution C 1s of GO (g), GO@P (h) and GO@H (i), GO-AgNPs (j), GO-AgNPs@P (k) and GO-AgNPs@H (l). XPS chemistry elemental analysis in high-resolution of Ag 3d spectra of GO-AgNPs (m), GO-AgNPs@P (n) and GO-AgNPs@H (o). XPS: X-ray photoelectron spectroscopic, NMs: nanomaterials, SD: standard deviation.

surfaces in the NMs@biocorona complexes, the signals from biomolecules suppress the intensity of the signal from molecular vibration characteristics of GO sheets. A significant difference was observed in the ATR-FTIR spectrum of the NMs@biocorona (Figure 4). Both NMs@biocorona complexes and protein controls (plasma proteins and hemolysate) showed a peak between 3500 to 3100 cm^{-1}, corresponding to the stretching of symmetrical and asymmetrical N–H bonds of amide A vibrations, and primary amine groups from proteins. Further, in the region between 3800 to 3100 cm^{-1} the O–H stretching contributes to the appearance of large and intense vibrational peaks, on the NMs@biocorona samples.[48] The bands between 2990 to 2770 cm^{-1} correspond to C–H symmetric and

6 of 14

J. Braz. Chem. Soc. **2024**, *35*, 12, e-20240148
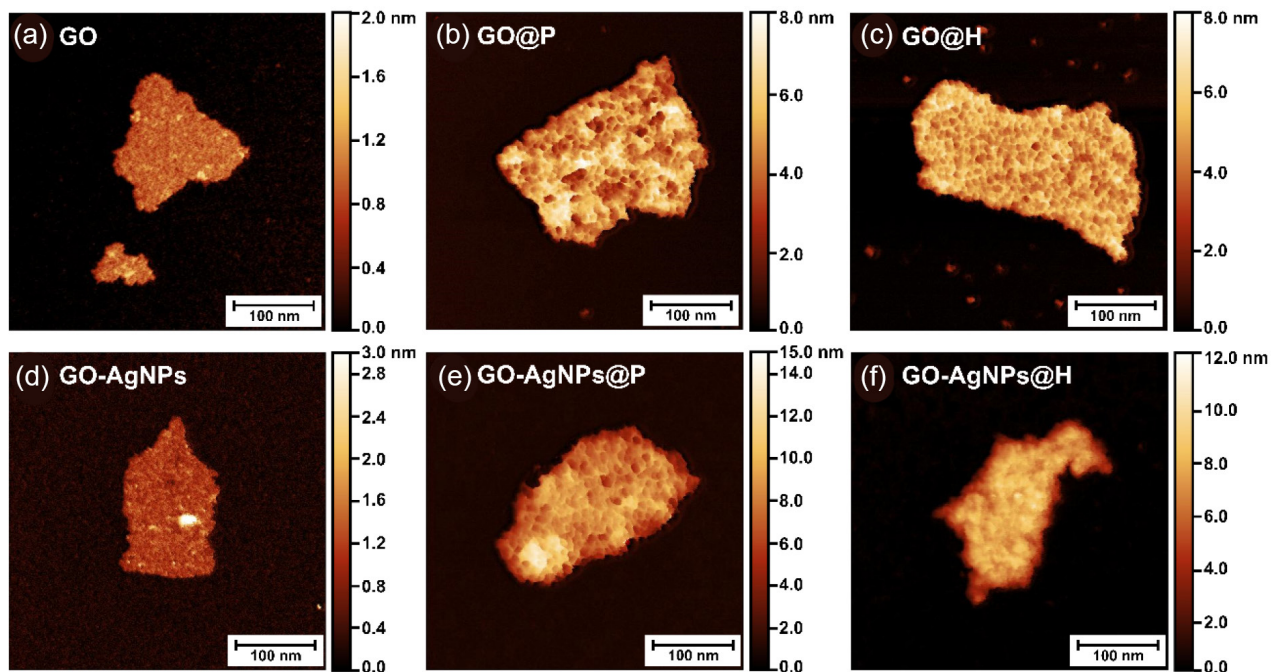
Figure 3. Surface characterization by atomic force microscopy (AFM). Topographic images of GO (a), GO@P (b), GO@H (c), GO-AgNPs (d), GO-AgNPs@P (e) and GO-AgNPs@H (f).

asymmetric stretching vibration of CH_2 and CH_3 groups, attributed to the aliphatic chains.[49,50] In the protein controls, the peaks at 1650 and 1540 cm^{-1} correspond to the C=O stretching and N–H bending of amide I and amide II protein components, respectively.[51] The peaks at the region between 1600 to 1790 cm^{-1} correspond to C=O stretching of carboxylic acids and esters functions, of GO surface and amide groups from protein controls on NMs@biocorona samples. The bands between 1449 to 1420 cm^{-1} correspond to NH_2, CH_2, and CH_3 bending vibrations.[52,53] The range from 1400 to 700 cm^{-1} shows bands observed especially in the plasma proteins control, corresponding to CH_3 deformation of aliphatic side groups, C–O stretching, and C=C bending vibrations assigned to amino acid residues.[54-57] In this sense, the ATR-FTIR characterization of NMs@biocorona complexes confirms the chemical changes in NMs after the biocorona formation, which is mainly observed by the suppression of the intensity of vibrational modes characteristic of GO/GO-AgNPs sheets and the appearance of signals similar to the protein controls, the signals from the molecular vibrations of nitrogenated and aliphatic organic groups, from the plasma and hemolysate biomolecules. The functionalization of GO and GO-AgNPs with plasma proteins is very pronounced, as highlighted by the intensity of the C–O stretching peak at 1000 cm^{-1} in both spectra (plasma, GO@P, and GO-AgNPs@P samples), confirming the strong adsorption of these biomolecules in the NMs.
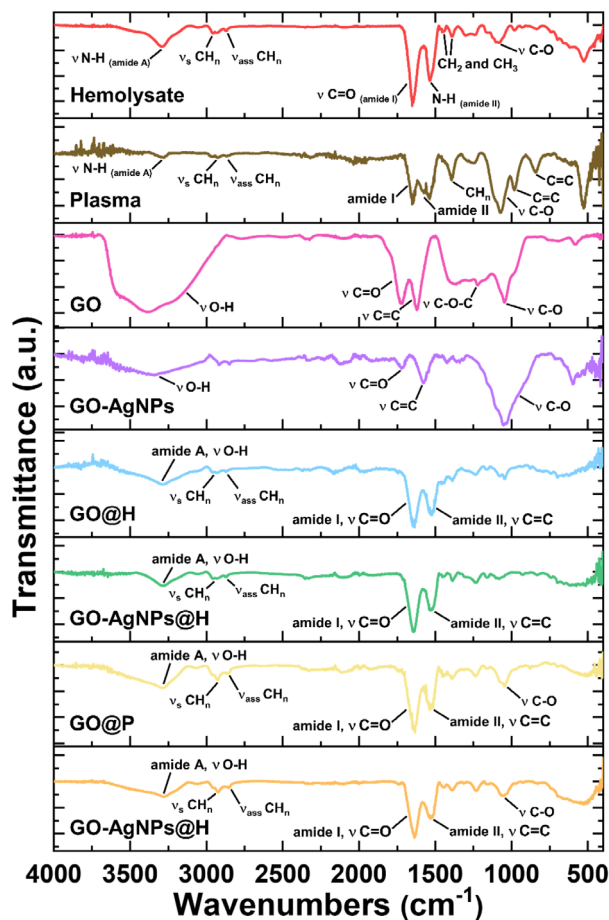
Figure 4. Attenuated total reflectance with Fourier transform infrared spectroscopy (ATR-FTIR) spectrum of hemolysate, plasma proteins, GO and GO-AgNPs in absence and presence of biocorona.

Colloidal stability in ultrapure water and phosphate-buffered saline

According to OECD (Organization for Economic Co-operation and Development) guideline No. 318,[58] dispersions that maintain their relative absorbance (A/A_0; final absorbance in relation to initial absorbance) > 90% throughout the monitored time in the test medium are considered to have a high dispersion stability. Dispersions with A/A_0 10% < and < 90% are considered to have an intermediate dispersion stability. Whereas dispersions with $A/A_0 \leq 10\%$ are considered to have a low dispersion stability.[58] Thus, the colloidal stability of GO and GO-AgNPs was evaluated in UPW and PBS.

The visual aspects and absorption data in the UPW showed that all studied samples, except the GO-AgNPs@H, maintained the A/A_0 > 90% during 1 h (high stability dispersions). GO-AgNPs@H was an intermediate dispersion-stable suspension, showing A/A_0 of approximately 20% after 1 h (Figures 5a and 5b). Hemolysate is a complex mixture of biomolecules, including lipophilic molecules, such as membrane lipoproteins and lipids. The GO-AgNPs@H exhibited low colloidal stability in UPW compared to the bare GO-AgNPs, which may indicate that the adsorbed biomolecules from hemolysate reduced the hydrophilicity of these NMs. The possible adsorption of lipophilic molecules from hemolysate can turn the effective solvation in the colloidal interactions between the water molecules and NMs hydrophilic surface into an unstable colloidal dispersion of GO-AgNPs covered with lipophilic hemolysate biomolecules, which explain the observed colloidal profile to this samples.[59,60]

PBS was used in the hemolysis assay to keep the integrity of the RBCs due to osmotic balance. Therefore, stability in this media was also assessed. The PBS (pH 7.3 to 7.5) used in the assays contains PO_4^{3-} (10 mmol L^{-1}) and NaCl, (150 mmol L^{-1}). The colloidal stability can be affected by NMs concentration, pH and medium salinity that may induce aggregation or sedimentation, consequently modulating the NMs bioavailability.[61-63] The GO, GO@P and GO@H in PBS maintained a high stability over 1 h, showing A/A_0 > 90%. However, GO-AgNPs exhibited low stability ($A/A_0 \leq 10\%$) in PBS, whereas the biocorona in GO-AgNPs@P and GO-AgNPs@H showed intermediate stability, causing a small improvement on the colloidal stability of GO-AgNPs (Figures 5c and 5d). The physicochemical characterization demonstrated that the GO-AgNPs has a lower concentration of oxygenated
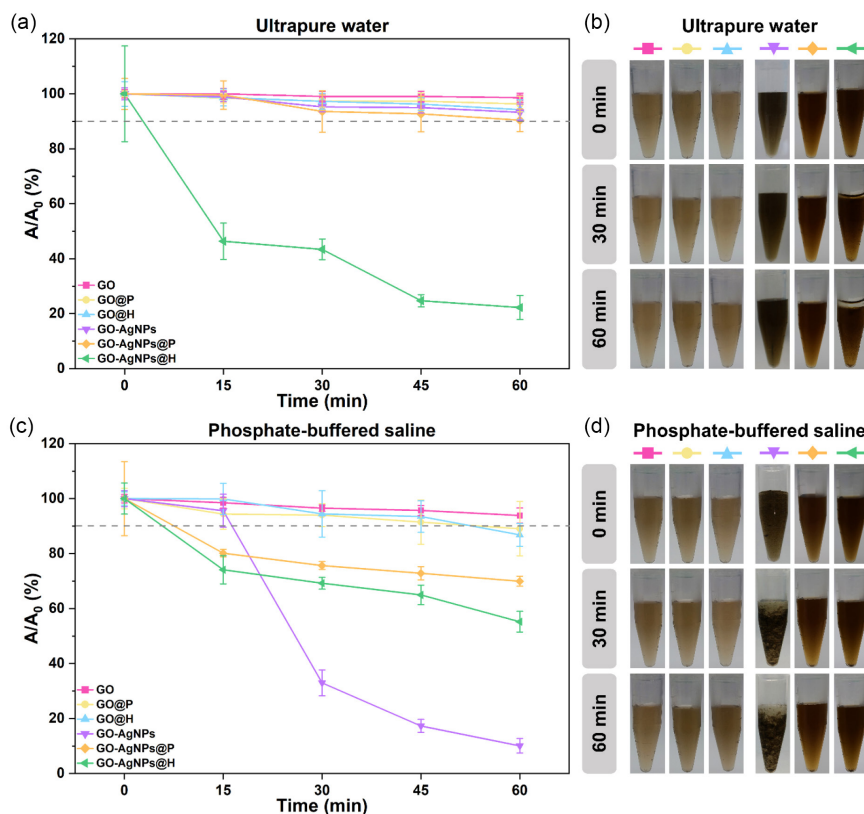
Figure 5. Percentage of NMs in suspension relative to initial absorbance (at 400 nm) of GO and GO-AgNPs (in the absence and presence of the biocorona) stability in UPW (a) and PBS (c). Visual inspection of the samples in UPW (b) and PBS (d) for 1 h. NMs: nanomaterials, UPW: ultrapure water, PBS: phosphate-buffered saline.

groups on the surface. The electrostatic charge density of the GO originates from the presence of the –COOH and C–OH surface groups.[64] In the PBS saline condition, the high concentration of ions in the solution neutralizes the charge density arising from the oxygenated groups of the GO sheets. Since GO-AgNPs already have a lower concentration of surface charges, the charge neutralization effect due to the high ionic concentration of the saline condition reduces the colloidal stability of these NMs. As expected, this effect is much less pronounced for bare GO, which has a high concentration of oxygenated groups on the surface.

Hemolytic assays

The hemolysis assay demonstrated that both GO and GO-AgNPs have a dose-dependent hemolytic effect. At 150 µg mL^{-1} GO-AgNPs cause approximately three times more Hb release than GO, causing 88 and 27% hemolysis, respectively (Figures 5a and 5c). Studies showed that the hemolytic effect of GO can be attributed to the different mechanistic pathways, which may be correlated to the oxidation degree of GO sheets. For example, GO can induce ROS production, resulting in lipid peroxidation (LPO) and consequently decreasing RBCs membrane integrity. However, those mechanisms are still not completely elucidated.[65-69] Another toxic mode of action that may induce cell rupture is the mechanical effect caused by the direct contact of RBCs with the sharp ends present in the GO flakes.[70,71] The interaction between GO and the cell membrane was demonstrated by Duan *et al.*,[72] which showed that GO interacts with the phospholipids in the cell bilayer membrane, causing disruption, and consequently breaking the cell membrane

Regarding GO-AgNPs nanohybrid, the hemolysis could be attributed to the addition or synergistic effect of the counterparts (GO and AgNPs). The AgNPs could trigger hemolysis by inducing pore membrane and LPO, modifying the membrane integrity, and leading to osmose lysis. Moreover, AgNPs could ionize and release Ag$^+$, which tends to increase the hemolytic effect as it can trigger the scrambling of the membrane and lead to cell disruption.[73-75]

Furthermore, the hemolytic effect of NM@biocorona was drastically reduced, causing less than 5% of hemolysis (Figure 6).[76,77] de Sousa *et al.*[78] and de Sousa Maia *et al.*[79] also studied the hemolytic effect of GO coated with biocorona, and in both studies the biocorona causes a decrease on the hemolysis. The mechanisms behind the toxicity reduction after biocorona formation are not completely elucidated yet. However, the data obtained by the ATR-FTIR and XPS techniques showed that the biocorona formed on the NMs induces surface chemical
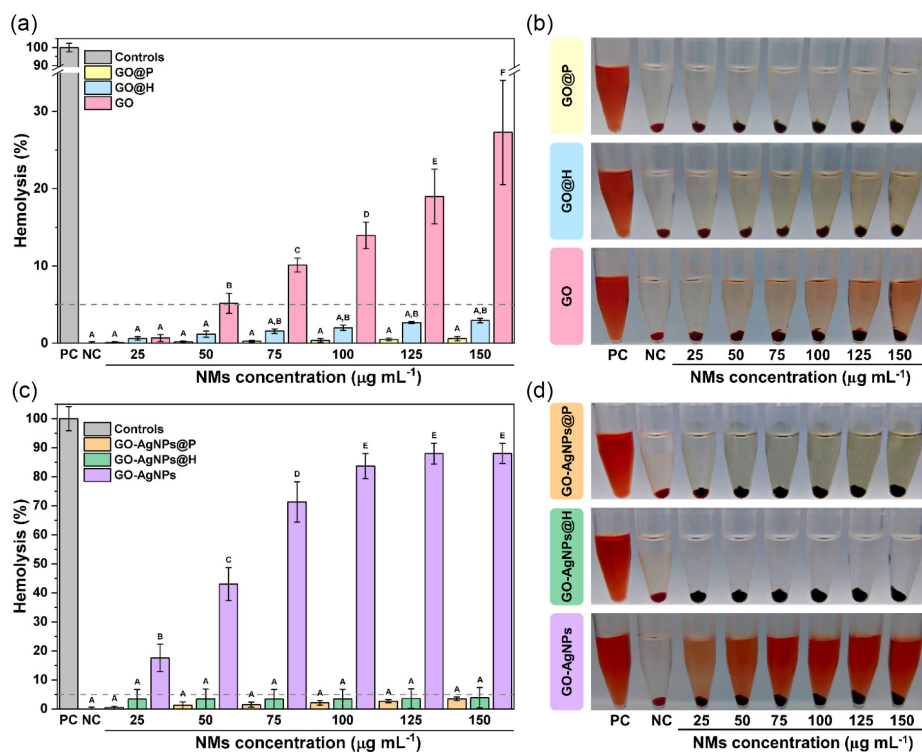
Figure 6. Percentage of hemolysis induced by GO (a) and GO-AgNPs (c) exposure in the absence and presence of the biocorona. Two-way ANOVA followed by Tukey's *post hoc* test; different letters indicate significant differences ($p < 0.05$). Visual inspection of GO (b) and GO-AgNPs (d) after 1 h exposure to 37 °C in the absence and presence of the biocorona.

changes on the GO and GO-AgNPs, which is emphasized by the presence of nitrogenous groups and increase of the C/O intensity ratio on NMs@biocorona. According to Martinez *et al.*,[80] the biocorona efficiently coats the surface of these NMs and acts as a barrier, decreasing the interaction between the chemical surface of NMs and the RBCs, reducing their hemolytic effects.

Monitoring of erythrocyte membrane morphology after interaction with nanomaterials

The RBCs morphology plays a fundamental role in gas transportation and distribution to the tissues of the body (O_2 and CO_2). Changes in this conformation can result in hypoxia and consequently clinical manifestations.[81] Thus, morphological modifications in the erythrocyte membrane caused by NMs can be used as a relevant toxicity biomarker.[70]

HQPCM images showed the GO and GO-AgNPs ($100 \, \mu g \, mL^{-1}$) cause a significant increase in RBCs diameter (Figures 7a and 7b), except for GO@P, which can be related to an impairment in the cell osmotic regulation, as well as imbalance on volume-regulated ion transport pathways or inability to repairs mechanic damages to cell membrane.[82,83] Furthermore, RBCs morphology analyzes conducted by Wang *et al.*[84] demonstrated that changes in cell volume are correlated with the beginning of the apoptotic process, as

well as the effect of oxidative stress. Therefore, although the biocorona mitigation the hemolytic effect, changes in erythrocyte morphology may occur. However, this was not observed for GO@P, for which the hemolytic effect is comparable to the control, causing 0,3% of hemolysis at a concentration of $100 \, \mu g \, mL^{-1}$ (Figure 6a). Adsorption results showed that GO has a high affinity to plasma proteins, adsorbing a significantly larger amount when compared with hemolysate.

When toxic effects occur in RBCs morphological, changes can occur due to interactions with membrane phospolipids.[85] A cell biomarker for hemolysis is called spherocytes, and this cell type occurs when there is a structural destabilization and lipid loss in the RBCs membrane. Also, interactions with the phospholipids in the RBCs bilayer membrane can induce the expansion of the outer layer, forming sharp projections on the membrane called echinocytosis or acanthocytosis, while interaction with the inner layer induces membrane invaginations forming stomatocytes.[86,87] Thus, the RBCs was evaluated by SEM looking for these alterations. Data obtained showed that the main erythrocyte morphological changes observed after exposed to GO was stomatocytes, spherocytes and echinocytes (or acanthocytes; Figures 8b-8d). Additionally, for GO@P and GO@H, the presence of echinocytes was also observed. For GO-AgNPs exposures, mainly spherocytes and stomatocytes were observed, with some spherocytes
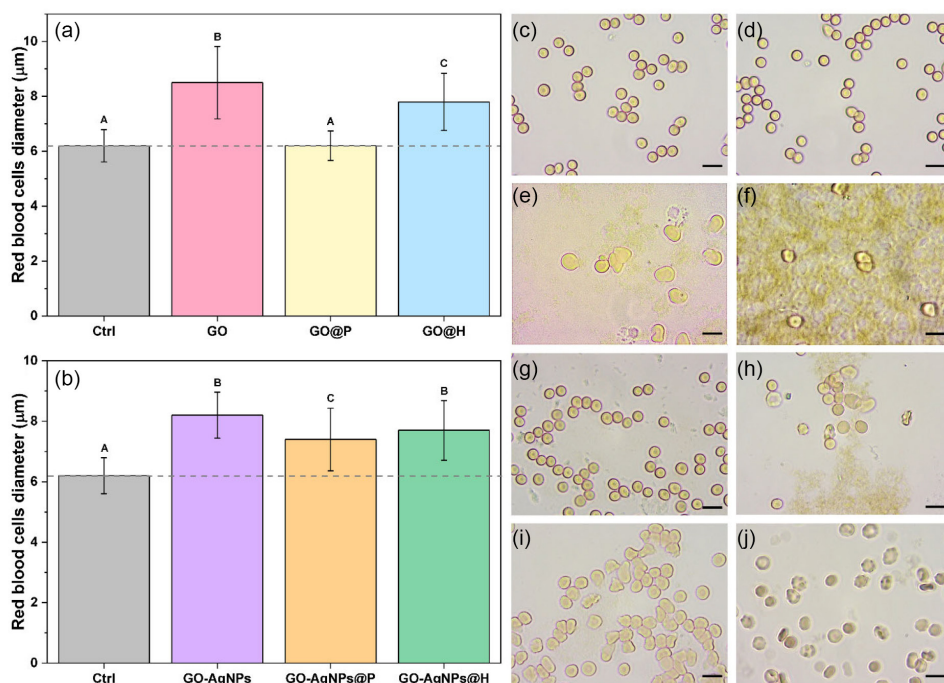
Figure 7. Evaluation of the RBCs morphology by HQPCM. RBCs diameter after exposure with GO (a) and GO-AgNPs (b) in absence and presence of biocorona. Kruskal-Wallis non-parametric test followed by Dunn's *post hoc* test; different letters indicate significant differences ($p < 0.05$). Optical images of RBCs control (c and d) and RBCs after exposure with $100 \, \mu g \, mL^{-1}$ of GO (e), GO-AgNPs (f), GO@P (g), GO-AgNPs@P (h), GO@H (i) and GO-AgNPs@H (j). Scale bar: 10 µm. RBCs: red blood cells, HQPCM: high-quality phase contrast microscopy.

10 of 14

J. Braz. Chem. Soc. **2024**, *35*, 12, e-20240148

and echinocytes being observed in GO-AgNPs@P and echinocytes in GO-AgNPs@H (Figures 8e-8g). The RBCs morphological changes observed corroborate with the results reported in the "Hemolytic assays" sub-section and the hypothesis that the hemolytic potential of the NMs studied can be attributed to interactions with erythrocyte

membrane components, which consequently causes their lysis.

Conclusions

Our study underscores the necessity of assessing the toxicity of GO-AgNPs, particularly on red blood cells, and examining their interactions with blood biomolecules. The hemolysis assay demonstrated that both GO and GO-AgNPs have a dose-dependent hemolytic effect. However, GO-AgNPs cause approximately three times more hemoglobin release than GO. This difference is associated with synergism between GO and AgNPs. Biocorona plays a protective role on the toxicity of these materials, becoming the primary interface with red blood cell membrane, and modifying the surface chemistry with carbonaceous and nitrogenous groups over oxygenated ones, thus mitigating hemolysis. However, although the biocorona formation mitigated the hemolytic effect, adverse effects on erythrocyte morphology may occur yet. Understanding these nanobio-interactions provides valuable insights into designing safer strategies to minimize toxicity and risks associated with this nanohybrid for applications in biomedical nanotechnology.
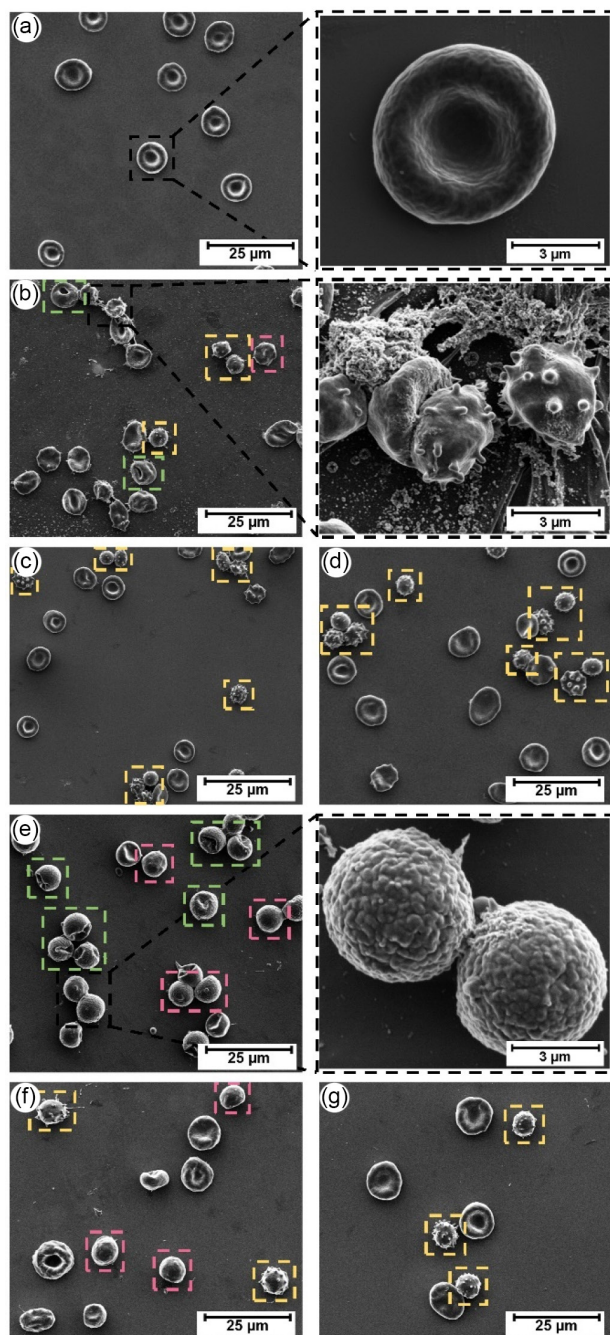
Supplementary Information

Supplementary data are available free of charge at http://jbcs.sbq.org.br as PDF file.

Acknowledgments

Figure 8. SEM images of untreated (a) and treated RBCs with 100 µg mL⁻¹ of GO (b), GO@P (c), GO@H (d), GO-AgNPs (e), GO-AgNPs@P (f) and GO-AgNPs@H (g). Areas of greater magnification in SEM images of untreated (a) and treated RBCs with GO (b) and GO-AgNPs (e) were highlighted by black dashed boxes. The dashed boxes highlighted in green, pink and yellow refer to stomatocytes, spherocytes and echinocytes (or acanthocytes).

Author Contributions

Nathalia C. L. Azevedo was responsible for conducting biological experiments and characterization of the NMs@biocorona, analyzing the data, and developing the manuscript; Aline M. Z. de Medeiros for the synthesis and characterization of the bare NMs (GO and GO-AgNPs) used in this work and analyzing the data; Gabriela H. da Silva and Fabrício S. Delite for training the research team,

References

1. Chung, C.; Kim, Y. K.; Shin, D.; Ryoo, S. R.; Hong, B. H.; Min, D. H.; *Acc. Chem. Res.* **2013**, *46*, 2211. [Crossref]

2. Ren, W.; Cheng, H. M.; *Nat. Nanotechnol.* **2014**, *9*, 726. [Crossref]

3. Dideikin, A. T.; Vul', A. Y.; *Front. Phys.* **2019**, *6*, 149. [Crossref]

4. Dreyer, D. R.; Park, S.; Bielawski, C. W.; Ruoff, R. S.; *Chem. Soc. Rev.* **2010**, *39*, 228. [Crossref]

5. Castro Neto, A. H.; Guinea, F.; Peres, N. M. R.; Novoselov, K. S.; Geim, A. K.; *Rev. Mod. Phys.* **2009**, *81*, 109. [Crossref]

6. Xu, M.; Zhu, J.; Wang, F.; Xiong, Y.; Wu, Y.; Wang, Q.; Weng, J.; Zhang, Z.; Chen, W.; Liu, S.; *ACS Nano* **2016**, *10*, 3267. [Crossref]

7. Fonseca, L. C.; de Araújo, M. M.; de Moraes, A. C. M.; da Silva, D. S.; Ferreira, A. G.; Franqui, L. S.; Martinez, D. S. T.; Alves, O. L.; *Appl. Surf. Sci.* **2018**, *437*, 110. [Crossref]

8. Yin, P. T.; Shah, S.; Chhowalla, M.; Lee, K. B.; *Chem. Rev.* **2015**, *115*, 2483. [Crossref]

9. Hassandoost, R.; Pouran, S. R.; Khataee, A.; Orooji, Y.; Joo, S. W.; *J. Hazard. Mater.* **2019**, *376*, 200. [Crossref]

10. Wang, D.; Saleh, N. B.; Sun, W.; Park, C. M.; Shen, C.; Aich, N.; Peijnenburg, W. J. G. M.; Zhang, W.; Jin, Y.; Su, C.; *Environ. Sci. Technol.* **2019**, *53*, 7265. [Crossref]

11. de Medeiros, A. M. Z.; Khan, L. U.; da Silva, G. H.; Ospina, C. A.; Alves, O. L.; de Castro, V. L.; Martinez, D. S. T.; *Ecotoxicol. Environ. Saf.* **2021**, *209*, 111776. [Crossref]

12. Zhou, Y.; Chen, R.; He, T.; Xu, K.; Du, D.; Zhao, N.; Cheng, X.; Yang, J.; Shi, H.; Lin, Y.; *ACS Appl. Mater. Interfaces* **2016**, *8*, 15067. [Crossref]

13. de Moraes, A. C. M.; Araujo Lima, B.; de Faria, A. F.; Brocchi, M.; Alves, O. L.; *Int. J. Nanomed.* **2015**, *10*, 6847. [Crossref]

14. de Faria, A. F.; Martinez, D. S. T.; Meira, S. M. M.; de Moraes, A. C. M.; Brandelli, A.; Souza Filho, A. G.; Alves, O. L.; *Colloids Surf., B* **2014**, *113*, 115. [Crossref]

15. Krishnaraj, C.; Kaliannagounder, V. K.; Rajan, R.; Ramesh, T.; Kim, C. S.; Park, C. H.; Liu, B.; Yun, S. I.; *Environ. Res.* **2022**, *210*, 112864. [Crossref]

16. Chen, J.; Zhao, Q.; Peng, J.; Yang, X.; Yu, D.; Zhao, W.; *J. Dent.* **2020**, *96*, 103332. [Crossref]

17. Ko, K.; Kim, M. J.; Lee, J. Y.; Kim, W.; Chung, H.; *Sci. Total Environ.* **2019**, *651*, 1087. [Crossref]

18. Mariadoss, A. V. A.; Saravanakumar, K.; Sathiyaseelan, A.; Wang, M. H.; *J. Photochem. Photobiol., B* **2020**, *210*, 111984. [Crossref]

19. Malik, S. B.; Saggu, J. I.; Gul, A.; Abbasi, B. A.; Iqbal, J.; Waris, S.; Jardan, Y. A. B.; Chalgham, W.; *Molecules* **2022**, *27*, 5184. [Crossref]

20. He, K.; Zeng, Z.; Chen, A.; Zeng, G.; Xiao, R.; Xu, P.; Huang, Z.; Shi, J.; Hu, L.; Chen, G.; *Small* **2018**, *14*, 1800871. [Crossref]

21. Zhou, X.; Dorn, M.; Vogt, J.; Spemann, D.; Yu, W.; Mao, Z.; Estrela-Lopis, I.; Donath, E.; Gao, C.; *Nanoscale* **2014**, *6*, 8535. [Crossref]

22. Tang, J.; Chen, Q.; Xu, L.; Zhang, S.; Feng, L.; Cheng, L.; Xu, H.; Liu, Z.; Peng, R.; *ACS Appl. Mater. Interfaces* **2013**, *5*, 3867. [Crossref]

23. Tsatsakis, A.; Stratidakis, A. K.; Goryachaya, A. V.; Tzatzarakis, M. N.; Stivaktakis, P. D.; Docea, A. O.; Berdiaki, A.; Nikitovic, D.; Velonia, K.; Shtilman, M. I.; Rizos, A. K.; Kuskov, A. N.; *Food Chem. Toxicol.* **2019**, *127*, 42. [Crossref]

24. de la Harpe, K.; Kondiah, P.; Choonara, Y.; Marimuthu, T.; du Toit, L.; Pillay, V.; *Cells* **2019**, *8*, 1209. [Crossref]

25. Simak, J.; de Paoli, S.; *Wiley Interdiscip. Rev.: Nanomed. Nanobiotechnol.* **2017**, *9*, e1448. [Crossref]

26. Anderson, N. L.; Anderson, N. G.; *Mol. Cell. Proteomics* **2002**, *1*, 845. [Crossref]

27. Aggarwal, P.; Hall, J. B.; McLeland, C. B.; Dobrovolskaia, M. A.; McNeil, S. E.; *Adv. Drug Delivery Rev.* **2009**, *61*, 428. [Crossref]

28. Owen, J. S.; McIntyre, N.; *Biochim. Biophys. Acta, Biomembr.* **1978**, *510*, 168. [Crossref]

29. Rice-evans, c.; Chapman, D.; *Scand. J. Clin. Lab. Invest.* **1981**, *41*, 99. [Crossref]

30. Franqui, L. S.; de Farias, M. A.; Portugal, R. V.; Costa, C. A. R.; Domingues, R. R.; Souza Filho, A. G.; Coluci, V. R.; Leme, A. F. P.; Martinez, D. S. T.; *Mater. Sci. Eng., C* **2019**, *100*, 363. [Crossref]

31. Monopoli, M. P.; Åberg, C.; Salvati, A.; Dawson, K. A.; *Nat. Nanotechnol.* **2012**, *7*, 779. [Crossref]

32. Kopac, T.; *Int. J. Biol. Macromol.* **2021**, *169*, 290. [Crossref]

33. Paula, A. J.; Martinez, D. S. T.; Araujo Júnior, R. T.; Souza Filho, A. G.; Alves, O. L.; *J. Braz. Chem. Soc.* **2012**, *23*, 1807. [Crossref]

34. Dawson, K. A.; Yan, Y.; *Nat. Nanotechnol.* **2021**, *16*, 229. [Crossref]

35. Al-Badri, M. A.; Smith, P.; Al-Jamal, K. T.; Lorenz, C. D.; *Adv. Mater. Interfaces* **2022**, *9*, 2101236. [Crossref]

36. Nel, A. E.; Mädler, L.; Velegol, D.; Xia, T.; Hoek, E. M. V.; Somasundaran, P.; Klaessig, F.; Castranova, V.; Thompson, M.; *Nat. Mater.* **2009**, *8*, 543. [Crossref]

12 of 14

J. Braz. Chem. Soc. **2024**, *35*, 12, e-20240148

37. de Luna, L. A. V.; Martinez, D. S. T.; Alves, O. L. In *Nanotoxicology: Materials, Methodologies, and Assessments*; Durán, N.; Guterres, S.; Alves, O. L., eds.; Springer: New York, 2014. [Link] accessed in July 2024

38. Dobrovolskaia, M. A.; Clogston, J. D.; Neun, B. W.; Hall, J. B.; Patri, A. K.; McNeil, S. E.; *Nano Lett.* **2008**, *8*, 2180. [Crossref]

39. ASTM E2524-08: *Standard Test Method for Analysis of Hemolytic Properties of Nanoparticles*, 2008.

40. ISO/TR 13014:2012: *Nanotechnologies - Guidance on Physico-Chemical Characterization of Engineered Nanoscale Materials for Toxicologic Assessment*, 2015.

41. Rahman, M.; Laurent, S.; Tawil, N.; Yahia, L.; Mahmoudi, M.; *Protein-Nanoparticle Interactions: The Bio-Nano Interface*, vol. 15, 1st ed.; Springer: Berlin, 2013. [Link] accessed in July 2024

42. Nečas, D.; Klapetek, P.; *Gwyddion*, version 2.61; Czech Metrology Institute, Czech Republic, 2022.

43. Rasband, W.; *ImageJ*, 2.0.0-rc-3; National Institutes of Health, Bethesda, MD, USA, 2014.

44. Geekiyanage, N. M.; Balanant, M. A.; Sauret, E.; Saha, S.; Flower, R.; Lim, C. T.; Gu, Y.; *PLoS One* **2019**, *14*, e0215447. [Crossref]

45. *OriginPro*, version 9.95 (2022b); OriginLab Corporation, Northampton, MA, USA, 2022.

46. Gignac, G. E.; *How2statsbook*, Australia, 2023. [Link] accessed in July 2024

47. Hu, W.; Peng, C.; Lv, M.; Li, X.; Zhang, Y.; Chen, N.; Fan, C.; Huang, Q.; *ACS Nano* **2011**, *5*, 3693. [Crossref]

48. Brzeska, J.; Elert, A.; Morawska, M.; Sikorska, W.; Kowalczuk, M.; Rutkowska, M.; *Polymers* **2018**, *10*, 826. [Crossref]

49. Zhang, Y. M.; Zhao, Q.; Li, L.; Yan, R.; Zhang, J.; Duan, J. C.; Liu, B. J.; Sun, Z. Y.; Zhang, M. Y.; Hu, W.; Zhang, N. N.; *RSC Adv.* **2018**, *8*, 32252. [Crossref]

50. Nandiyanto, A. B. D.; Oktiani, R.; Ragadhita, R.; *Indones. J. Sci. Technol.* **2019**, *4*, 97. [Crossref]

51. Crocco, M. C.; Moyano, M. F. H.; Annesi, F.; Bruno, R.; Pirritano, D.; Del Giudice, F.; Petrone, A.; Condino, F.; Guzzi, R.; *Sci. Rep.* **2023**, *13*, 2565. [Crossref]

52. Bertuoli, P. T.; Piazza, D.; Scienza, L. C.; Zattera, A. J.; *Appl. Clay Sci.* **2014**, *87*, 46. [Crossref]

53. Li, Z.; Pan, Z.; Wang, Y.; *Environ. Sci. Pollut. Res.* **2019**, *26*, 11126. [Crossref]

54. Martinez, D. S. T.; da Silva, G. H.; de Medeiros, A. M. Z.; Khan, L. U.; Papadiamantis, A. G.; Lynch, I.; *Nanomaterials* **2020**, *10*, 1936. [Crossref]

55. Ji, Y.; Yang, X.; Ji, Z.; Zhu, L.; Ma, N.; Chen, D.; Jia, X.; Tang, J.; Cao, Y.; *ACS Omega* **2020**, *5*, 8572. [Crossref]

56. Malek, K.; Wood, B. R.; Bambery, K. R. In *Optical Spectroscopy and Computational Methods in Biology and Medicine*, vol. 14; Baranska, M., eds.; Springer: Dordrecht, 2014, p. 419. [Link] accessed in July 2024

57. Giuliano, S.; Mistek-Morabito, E.; Lednev, I. K.; *ACS Omega* **2020**, *5*, 27026. [Crossref]

58. Organization for Economic Co-operation and Development (OECD); Test No. 318: *Dispersion Stability of Nanomaterials in Simulated Environmental Media*, USA, 2017.

59. Salvioli, G.; Rioli, G.; Lugli, R.; Salati, R.; *Gut* **1978**, *19*, 844. [Crossref]

60. Kozlova, E.; Chernysh, A.; Moroz, V.; Sergunova, V.; Gudkova, O.; Manchenko, E.; *Sci. Rep.* **2017**, *7*, 7846. [Crossref]

61. Afshinnia, K.; Baalousha, M.; *Sci. Total Environ.* **2017**, *581-582*, 268. [Crossref]

62. Su, Y.; Yang, G.; Lu, K.; Petersen, E. J.; Mao, L.; *Environ. Pollut.* **2017**, *220*, 469. [Crossref]

63. Pavani, P.; Kumar, K.; Rani, A.; Venkatesu, P.; Lee, M. J.; *J. Mol. Liq.* **2021**, *331*, 115753. [Crossref]

64. Gudarzi, M. M.; *Langmuir* **2016**, *32*, 5058. [Crossref]

65. Liao, W.; Chen, L.; Ma, X.; Jiao, R.; Li, X.; Wang, Y.; *Eur. J. Med. Chem.* **2016**, *114*, 24. [Crossref]

66. Palmieri, V.; Perini, G.; de Spirito, M.; Papi, M.; *Nanoscale Horiz.* **2019**, *4*, 273. [Crossref]

67. Fedel, M.; *C--Open Access Carbon Res. J.* **2020**, *6*, 12. [Crossref]

68. Li, R.; Guiney, L. M.; Chang, C. H.; Mansukhani, N. D.; Ji, Z.; Wang, X.; Liao, Y. P.; Jiang, W.; Sun, B.; Hersam, M. C.; Nel, A. E.; Xia, T.; *ACS Nano* **2018**, *12*, 1390. [Crossref]

69. Zhang, J.; Cao, H. Y.; Wang, J. Q.; Wu, G. D.; Wang, L.; *Front. Cell. Dev. Biol.* **2021**, *9*, 616888. [Crossref]

70. Liao, K. H.; Lin, Y. S.; Macosko, C. W.; Haynes, C. L.; *ACS Appl. Mater. Interfaces* **2011**, *3*, 2607. [Crossref]

71. Kenry; *J. Mater. Res.* **2018**, *33*, 44. [Crossref]

72. Duan, G.; Kang, S.; Tian, X.; Garate, J. A.; Zhao, L.; Ge, C.; Zhou, R.; *Nanoscale* **2015**, *7*, 15214. [Crossref]

73. Choi, J.; Reipa, V.; Hitchins, V. M.; Goering, P. L.; Malinauskas, R. A.; *Toxicol. Sci.* **2011**, *123*, 133. [Crossref]

74. Sopjani, M.; Föller, M.; Haendeler, J.; Götz, F.; Lang, F.; *J. Appl. Toxicol.* **2009**, *29*, 531. [Crossref]

75. Chen, L. Q.; Fang, L.; Ling, J.; Ding, C. Z.; Kang, B.; Huang, C. Z.; *Chem. Res. Toxicol.* **2015**, *28*, 501. [Crossref]

76. Kwon, T.; Woo, H. J.; Kim, Y. H.; Lee, H. J.; Park, K. H.; Park, S.; Youn, B.; *J. Nanosci. Nanotechnol.* **2012**, *12*, 6168. [Crossref]

77. Papi, M.; Lauriola, M. C.; Palmieri, V.; Ciasca, G.; Maulucci, G.; de Spirito, M.; *RSC Adv.* **2015**, *5*, 81638. [Crossref]

78. de Sousa, M.; Martins, C. H. Z.; Franqui, L. S.; Fonseca, L. C.; Delite, F. S.; Lanzoni, E. M.; Martinez, D. S. T.; Alves, O. L.; *J. Mater. Chem. B* **2018**, *6*, 2803. [Crossref]

79. de Sousa Maia, D. L.; Côa, F.; da Silva, K. B.; Martins, C. H. Z.; Franqui, L. S.; Fonseca, L. C.; da Silva, D. S.; Delite, F. S.; Martinez, D. S. T.; Alves, O. L.; *J. Mater. Sci.* **2024**, *59*, 577. [Crossref]

80. Martinez, D. S. T.; Paula, A. J.; Fonseca, L. C.; Luna, L. A. V.; Silveira, C. P.; Durán, N.; Alves, O. L.; *Eur. J. Inorg. Chem.* **2015**, *2015*, 4595. [Crossref]

J. Braz. Chem. Soc. **2024**, *35*, 12, e-20240148

13 of 14

81. Mebius, R. E.; Kraal, G.; *Nat. Rev. Immunol.* **2005**, *5*, 606. [Crossref]

82. Klbik, I.; *Cryobiology* **2024**, *114*, 104795. [Crossref]

83. McNeil, P. L.; Terasaki, M.; *Nat. Cell Biol.* **2001**, *3*, E124. [Crossref]

84. Wang, D. C.; Chen, K. Y.; Tsai, C. H.; Chen, G. Y.; Chen, C. H.; *J. Biomech.* **2011**, *44*, 2790. [Crossref]

85. Villanueva-Flores, F.; Castro-Lugo, A.; Ramírez, O. T.; Palomares, L. A.; *Nanotechnology* **2020**, *31*, 132002. [Crossref]

86. Gallagher, P. G.; *Hematology Am. Soc. Hematol. Educ. Program.* **2005**, *1*, 13. [Crossref]

87. Bessis, M. In *Red Cell Shapes*; Bessis, M.; Weed, R. I.; Leblond, P. F., eds.; Springer: Berlin, 1973. [Crossref]

14 of 14

J. Braz. Chem. Soc. **2024**, *35*, 12, e-20240148